ANNUAL REVIEWS

Annual Review of Condensed Matter Physics

First-Principles Approaches to Magnetoelectric Multiferroics

Changsong Xu,[1,2] Hongyu Yu,[1,2] Junling Wang,[3,4] and Hongjun Xiang[1,2,5]

[1]Key Laboratory of Computational Physical Sciences (Ministry of Education), Institute of Computational Physical Sciences, State Key Laboratory of Surface Physics, and Department of Physics, Fudan University, Shanghai, China; email: hxiang@fudan.edu.cn

[2]Shanghai Qi Zhi Institute, Shanghai, China

[3]Department of Physics, Southern University of Science and Technology (SUSTech), Shenzhen, China

[4]Guangdong Provincial Key Laboratory of Functional Oxide Materials and Devices, Southern University of Science and Technology, Shenzhen, China

[5]Collaborative Innovation Center of Advanced Microstructures, Nanjing, China

Annu. Rev. Condens. Matter Phys. 2024. 15:85–108

First published as a Review in Advance on November 14, 2023

The *Annual Review of Condensed Matter Physics* is online at conmatphys.annualreviews.org

https://doi.org/10.1146/annurev-conmatphys-032922-102353

Keywords

magnetoelectric coupling, first-principles methods, effective Hamiltonian, machine learning potential

Abstract

Magnetoelectric multiferroics, which display both ferroelectric and magnetic orders, are appealing because of their rich fundamental physics and promising technological applications. The revival of multiferroics since 2003 led to a comprehensive understanding of the mechanisms that facilitate the coexistence of electric and magnetic orders and conceptually new design strategies for device architectures, which brought us an important step closer to multiferroic-based technology. In the past thirty years, first-principles calculations based on the laws of quantum mechanics played a crucial role in understanding the electronic, magnetic, and structural properties of multiferroics and guided the design of new multiferroics with improved properties. In this review, we provide a comprehensive overview of first-principles approaches to magnetoelectric multiferroics, especially in low-dimensional forms. In particular, we discuss methods to build an effective Hamiltonian from first principles for magnets, ferroelectrics, and multiferroics. The recently developed machine learning potential approach for multiferroics is also outlined. Furthermore, we present the unified model

for spin-induced ferroelectricity and methods for computing the linear magnetoelectric coupling tensor. Finally, recent progress in multiferroic systems and the applications of first-principles approaches to these systems are reviewed.

1. INTRODUCTION

In 1994, Schmid proposed the concept of multiferroic materials (1), which refers to single-phase compounds that exhibit two or more primary ferroic properties (ferromagnetism, ferroelectricity, ferroelasticity, or ferrotoroidicity). Among them, magnetoelectric (ME) multiferroics display a coupling between their electric and magnetic properties. Later, the initial concept of coexisting orders was expanded beyond just primary ferroic states to also include, e.g., antiferromagnetism, antiferroelectricity (2), and composite materials (3). In this review, we follow this modern definition when referring to multiferroics. Multiferroic materials have gained considerable attention due to their potential applications in next-generation electronic, data storage, and sensing technologies (4–10). The coupling between magnetic and electric properties of the same material is highly desirable for developing energy-efficient devices, such as magnetic memories that can be written electrically, and sensors that can detect magnetic fields with high sensitivity.

According to the microscopic sources of ferroelectricity, Khomskii suggested classifying multiferroic materials into two types (11). Type-I multiferroics refer to those materials in which ferroelectricity and magnetism originate from different ions and may couple to each through the lattice. Examples are perovskite $BiFeO_3$ (12) and hexagonal $YMnO_3$ (13). In the type-II multiferroics, the ferroelectricity is induced by certain magnetic orders that break the spatial inversion symmetry, implying a strong direct coupling between the two. For example, a spiral magnetic ordering appears below 28 K in $TbMnO_3$ (14), which simultaneously gives rise to a nonzero electric polarization.

In the field of multiferroics, first-principles methods [especially density functional theory (DFT)] have become crucial for understanding the fundamental mechanisms of multiferroic behavior and to guide experimental efforts to synthesize and characterize multiferroics. In 2000, Spaldin (then Hill) elaborated on the basis of first-principles calculations why, in classic perovskites, displacive ferroelectricity and magnetic order are working against each other (15). Later, the large electric polarization observed in thin films of $BiFeO_3$ (12), which appeared to be at odds with previous bulk single-crystal measurements, was reconciled by a DFT study (16) showing that bulk $BiFeO_3$ should indeed display a large spontaneous polarization of $\sim$95 $\mu C/cm^2$. First-principles calculations showed that ferroelectricity in $YMnO_3$ results from an interplay between a polar Γ-point mode and a nonpolar Brillouin zone–boundary mode that leads to a unit cell tripling (17). Ab initio calculations were also performed for type-II multiferroics, first on collinear antiferromagnets such as $TbMn_2O_5$ (18) and $HoMnO_3$ (19). Within the type-II multiferroics with noncollinear spin order, Li–Copper-based oxides were the first compounds to be studied from first principles (20). Shortly after, the prototypical case of $TbMnO_3$ was studied with first-principles methods by two groups (21, 22). It was shown that the purely electronic contribution was much smaller than the ionic contribution, and the magnitude and direction of the calculated polarization was found to be in excellent agreement with experiments (14). In terms of multiferroic composites, Duan et al. showed theoretically that a change in bonding at the ferroelectric–ferromagnet interface would alter the interface magnetization when the electric polarization reverses (23). Although multiferroics are nonmetallic by the original definition, it was

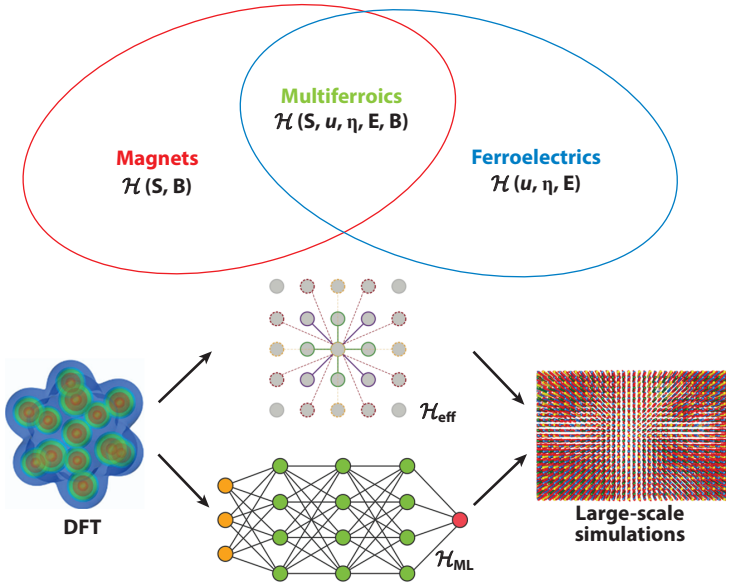

Figure 1

Multiferroics combine and couple the properties of magnets and ferroelectrics. The first-principles methods, involving many degrees of freedom, generate accurate total energy and electronic properties, but only for small systems (around or less than a hundred atoms) at zero temperature. By contrast, the effective Hamiltonian $\mathcal{H}_{\text{eff}}$ and Hamiltonian made with machine learning potentials $\mathcal{H}_{\text{ML}}$, which can be constructed from first-principles results and considers only limited degrees of freedom, enable large-scale thermal and dynamic simulations. A major difference between $\mathcal{H}_{\text{eff}}$ and $\mathcal{H}_{\text{ML}}$ is that the former has explicit forms of interactions, whereas the latter adopts implicit interactions. Abbreviation: DFT, density functional theory.

suggested (24) that a two-dimensional metallic system with an out-of-plane polarization may host ferromagnetic–ferroelectric multiferroicity.

This review aims at introducing the commonly used first-principles and first-principles-based methods in multiferroics. The calculations of magnetic, electric, and ME properties are discussed (see **Figure 1** for the scope of this review). Recent progress in multiferroics, especially those in two-dimensional forms, is also reviewed.

2. FIRST-PRINCIPLES TECHNIQUES RELATED TO MULTIFERROICS

First-principles calculations have significantly contributed to the progress in multiferroics by elucidating different mechanisms for multiferroicity, computing essential physical properties, and rationally designing high-performance multiferroics. Because the Hamiltonian (defined to be the sum of the kinetic and potential energies) of a system determines the thermodynamic properties and the kinetic behavior (even under external electric and/or magnetic fields), in this review we mainly focus on the construction of a Hamiltonian for multiferroics based on first-principles calculations and the use of a Hamiltonian to investigate the coupling between the magnetic and electric degrees of freedom. We describe in detail the effective Hamiltonian approach, which involves constructing a simplified Hamiltonian that captures the essential physics of the system while neglecting the details of the microscopic interactions that are not relevant to the phenomena of interest. Furthermore, we also briefly introduce the machine learning (ML) approach for constructing an atomistic Hamiltonian for multiferroics, which is expected to play a more important role in the theoretical studies on multiferroics in the near future.

2.1. Magnets

The magnetic properties of a material are determined by the exchange interactions between magnetic moments, which originate from the overlapping of magnetic ion orbitals, with or without intermediate nonmagnetic ions. Such exchange interactions can be captured by the Hubbard model (25) for electrons on a lattice site. A more convenient way is to adopt the effective spin Hamiltonian, which results from downfolding the Hubbard model and contains only spin degrees of freedoms. In this subsection, we first introduce the common forms of spin Hamiltonians and then discuss the first-principles methods for constructing such Hamiltonians.

Let us start with a complete form of bilinear coupling, which reads as

$$\mathcal{H}^{bl} = \sum_{<i,j>} \mathbf{S}_i \cdot \mathcal{J}_{ij} \cdot \mathbf{S}_j, \qquad 1.$$

where $\mathbf{S}(S_x, S_y, S_z)$ is a spin vector, and $\mathcal{J}$ is a 3×3 tensor with its explicit form expressed as

$$\mathcal{J} = \begin{pmatrix} J^{xx} & J^{xy} & J^{xz} \\ J^{yx} & J^{yy} & J^{yz} \\ J^{zx} & J^{zy} & J^{zz} \end{pmatrix}.$$

(*a*) In the simplest case, where the matrix $\mathcal{J}$ has no off-diagonal elements and all diagonal elements are the same, i.e., $J = J^{xx} = J^{yy} = J^{zz}$, the coupling becomes the isotropic Heisenberg interaction with the form of $J\mathbf{S}_i \cdot \mathbf{S}_j$.

(*b*) If the diagonal elements are not all the same, the coupling yields anisotropic exchange coupling. For example, in a tetragonal system, it can be $J^{xx} = J^{yy} \neq J^{zz}$. In a general case, the isotropic J is an average of the diagonal elements of $\mathcal{J}$, as $J = \frac{1}{3}(J^{xx} + J^{yy} + J^{zz})$. Another interesting example is the Kitaev interaction, for which the unique direction is bond-dependent. For honeycomb lattice and the $\{XYZ\}$ basis illustrated in **Figure 2**, the $\mathcal{J}$ matrices for X-, Y-, and Z-bond have the forms of

$$\begin{pmatrix} J+K & 0 & 0 \\ 0 & J & 0 \\ 0 & 0 & J \end{pmatrix} \begin{pmatrix} J & 0 & 0 \\ 0 & J+K & 0 \\ 0 & 0 & J \end{pmatrix} \begin{pmatrix} J & 0 & 0 \\ 0 & J & 0 \\ 0 & 0 & J+K \end{pmatrix}.$$

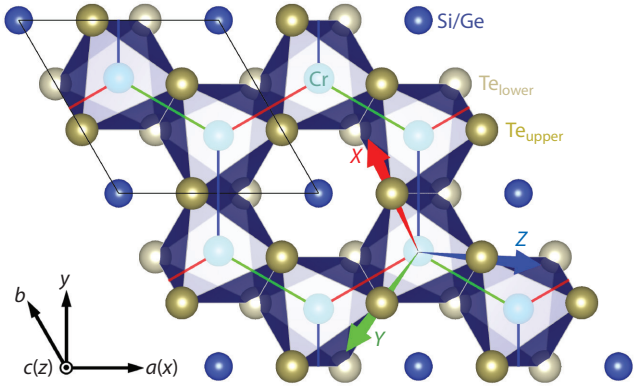

Figure 2

Schematics of crystal structure and the Kitaev basis of a $CrSiTe_3$ monolayer. The black parallelogram marks the unit cell of the honeycomb lattice. The material basis of $\{xyz\}$ is shown at bottom left. The Kitaev basis of $\{XYZ\}$ is indicated by red, green, and blue arrows. The X, Y, and Z directions are found to be very close to the Cr-Te bonds but are perpendicular to each other. Figure adapted with permission from Reference 26; copyright 2020 American Physical Society.

(*c*) A more complex case is to further introduce off-diagonal elements to the $\mathcal{J}$ matrix in the symmetric manner of $J^{xy} = J^{yx}$, $J^{xz} = J^{zx}$, and $J^{yz} = J^{zy}$. In such a case, the x, y, and z directions are no longer representative, and the eigen directions can be determined by diagonalization of the $\mathcal{J}$ matrix.

(*d*) Notably, the antisymmetric part of the $\mathcal{J}$ matrix, where $J^{xy} = -J^{yx}$, $J^{xz} = -J^{zx}$, and $J^{yz} = -J^{zy}$, corresponds to the Dzyaloshinskii–Moriya interaction (DMI) (27, 28). If expanding Equation 1 with an antisymmetric $\mathcal{J}$, and comparing with the typical DMI expression $\mathcal{H}_{\rm DM} = \mathbf{D}\cdot(\mathbf{S}_i \times \mathbf{S}_j)$, one can find that $D_x = \frac{1}{2}(J^{yz} - J^{zy})$, $D_y = \frac{1}{2}(J^{zx} - J^{xz})$, and $D_z = \frac{1}{2}(J^{xy} - J^{yx})$.

Note that all above forms other than the Heisenberg interaction are a consequence of the spin–orbit coupling (SOC). Another SOC effect is the single-ion anisotropy (SIA), which can be viewed as an exchange interaction between one site and itself. In the bilinear form, the SIA reads as

$$\mathcal{H}^{SIA} = \sum_i \mathbf{S}_i\cdot\mathcal{A}_{ii}\cdot\mathbf{S}_i, \qquad 2.$$

where $\mathcal{A}$ is a symmetric tensor. Note that only the energy difference among diagonal elements matters. Interestingly, it was discovered theoretically (29, 30) that spin-half or effective spin-half ions may have SIA in contrast to the usual belief (31), which agrees with a recent experiment (32).

More complex couplings include higher-order interactions, such as the two-site biquadratic interaction $B(\mathbf{S}_i\cdot\mathbf{S}_j)^2$ (33, 34), and many-body interactions, such as the four-site fourth-order interaction $C(\mathbf{S}_i\cdot\mathbf{S}_j)(\mathbf{S}_k\cdot\mathbf{S}_l)$ (35–37). Such many-body and higher-order interactions can also involve SOC effects and exhibit anisotropy (37).

In the following, we discuss the first-principles approaches (i.e., methods based on total energy and methods based on perturbation) to determine the aforementioned spin Hamiltonian and the coefficients therein.

2.1.1. Total energy–based methods. With a general form of Hamiltonian at hand, it is crucial to obtain the coefficients of different terms. Here, we introduce the total energy–based methods, which are straightforward and widely used.

2.1.1.1. Usual energy mapping method. The simplest method based on total energy for computing exchange interactions is the so-called energy mapping method (38, 39). Within this method, one adopts a predefined form of the spin Hamiltonian for a given material and chooses specific magnetic configurations to perform DFT calculations. By comparing the spin Hamiltonian energy expressions of these magnetic configurations with DFT total energies, one can obtain the exchange interaction parameters of the spin Hamiltonian via solving the linear equations.

Let us adopt the P4mm phase $BiFeO_3$ as an example (see **Figure 3*a***) to illustrate this method in more detail (40). Consider the following Hamiltonian:

$$\mathcal{H}^{\rm BiFeO_3} = \sum_{<i,j>_a} J_a\mathbf{S}_i\cdot\mathbf{S}_j + \sum_{<i,j>_c} J_c\mathbf{S}_i\cdot\mathbf{S}_j + \sum_{<i,j>_{ac}} J_{ac}\mathbf{S}_i\cdot\mathbf{S}_j, \qquad 3.$$

where J_a and J_c are both the first-nearest-neighbor coupling but along in-plane and out-of-plane directions, respectively, whereas J_{ac} is the second-nearest-neighbor interaction. To solve such a model, one needs a $2 \times 2 \times 2$ supercell and to construct four different spin configurations, as

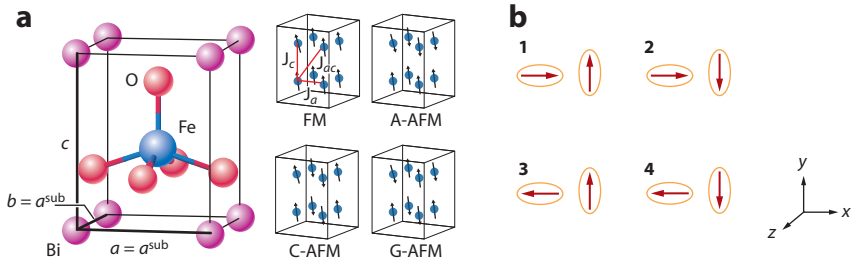

Figure 3

Examples of spin state settings for total energy–based methods. (*a*) The crystal structure of tetragonal $BiFeO_3$ in P4mm phase, as well as four different magnetic states, each within a 2 × 2 × 2 supercell. (*b*) Illustration of the four states of $\mathbf{S}_1$ and $\mathbf{S}_2$, which are used to calculate the J_{xy} component using the four-state method. Note that, in the case of J_{xy}, spins other than $\mathbf{S}_1$ and $\mathbf{S}_2$ are set to be along the *z* direction, with their configurations being as close as possible to the ground state. Panel *a* adapted with permission from Reference 40; copyright 2012 American Physical Society. Abbreviations: A-AFM, A-type antiferromagnetism; C-AFM, C-type antiferromagnetism; FM, ferromagnetism; G-AFM, G-type antiferromagnetism.

shown in **Figure 3*a***. Then, the energies of the four configurations can be expressed as

$$\begin{aligned} E_F &= E_0 + 2J_a + J_c + 4J_{ac} \\ E_A &= E_0 + 2J_a - J_c - 4J_{ac} \\ E_C &= E_0 - 2J_a + J_c - 4J_{ac} \\ E_G &= E_0 - 2J_a - J_c + 4J_{ac}, \end{aligned} \quad 4.$$

where energies on the left side can be obtained from DFT calculations, and E_0 is the energy that is not related to magnetism. Note that E_0 does not appear in Equation 3, as the nonmagnetic energy contribution is excluded in the spin Hamiltonian. By solving the linear equations in Equation 4, the J_a, J_b, and J_{ac} coefficients of Equation 3 can be determined.

In principle, the energy mapping approach can be generally adopted to estimate other magnetic interacting parameters (e.g., the DMI strength) (41, 42) besides the isotropic exchange parameters. However, the disadvantage of this approach is that for complicated magnetic systems it is hard to choose beforehand a plausible spin Hamiltonian and select appropriate magnetic configurations.

2.1.1.2. Four-state method. To resolve the deficiency of the usual energy mapping method, Xiang et al. proposed the four-state method (43, 44) to compute all the magnetic interacting parameters of any bilinear spin Hamiltonians. Consider the bilinear spin interaction between site 1 and site 2, which are located in a large magnetic system with other spins. The spin Hamiltonian of such a system can be written as

$$\mathcal{H} = E_0 + \sum_{<i,j>} \mathbf{S}_i \cdot \boldsymbol{J}_{ij} \cdot \mathbf{S}_j. \quad 5.$$

We can further separate the energy terms related to spins 1 and 2:

$$\mathcal{H} = \mathbf{S}_1 \cdot \mathcal{J}_{12} \cdot \mathbf{S}_2 + \mathbf{S}_1 \cdot \mathbf{K}_1 + \mathbf{S}_2 \cdot \mathbf{K}_2 + \mathcal{H}^{\text{other}}, \quad 6.$$

where the first term is the targeted interaction between site 1 and site 2, the second (third) term is the interactions between site 1 (2) and other spins, and the fourth term covers all the interactions among other spins. To calculate, e.g., the J^{xy} component of $\mathcal{J}_{12}$, four spin states (see **Figure 3*b***) are considered for the $\{\mathbf{S}_1, \mathbf{S}_2\}$ pair: $\{(S\,0\,0), (0\,S\,0)\}$, $\{(S\,0\,0), (0\,-S\,0)\}$, $\{(-S\,0\,0), (0\,S\,0)\}$, and $\{(-S\,0\,0),$

$(0\ -S\ 0)\}$; whereas other spins are perpendicular to both $\mathbf{S}_1$ and $\mathbf{S}_2$ (e.g., along the z direction). The J^{xy} can then be obtained with the energies from DFT calculations using the following equations:

$$\begin{aligned} E_1 &= +J^{xy}S^2 + S_1K_1 + S_2K_2 + E_{\text{other}} + E_0, \\ E_2 &= -J^{xy}S^2 + S_1K_1 - S_2K_2 + E_{\text{other}} + E_0, \\ E_3 &= -J^{xy}S^2 - S_1K_1 + S_2K_2 + E_{\text{other}} + E_0, \\ E_4 &= +J^{xy}S^2 - S_1K_1 - S_2K_2 + E_{\text{other}} + E_0, \\ J^{xy} &= (E_1 - E_2 - E_3 + E_4)/4S^2, \end{aligned} \qquad 7.$$

where E_{other} denotes the energy of spin interactions among spins other than $\mathbf{S}_1$ and $\mathbf{S}_2$. In a similar way, all the other elements of $\mathcal{J}$ can be obtained by performing DFT calculations on four specially designated magnetic states.

To correctly/better perform the four-state method, one needs to be careful with several aspects. (*a*) The four-state method is based on the scenario that $\mathbf{S}_1$ and $\mathbf{S}_2$ are isolated in a large system. To fulfill such a scenario in DFT calculations, a large enough supercell is required to prevent the coupling between targeted spins and their images in the periodically repeated supercells. (*b*) To obtain the $\mathcal{J}$ matrix, SOC should be turned on. Meanwhile, directions of all spins should be constrained, in case they deviate from the designed directions. If only the isotropic Heisenberg J parameter is needed, one can turn off SOC and noncollinear setting and simply consider the four states of $\{S, S\}$, $\{S, -S\}$, $\{-S, S\}$, and $\{-S, -S\}$. (*c*) According to the previous definition of DMI, one needs two elements to obtain a component of $\mathbf{D}$ vector, as $D_\alpha = \frac{1}{2}(J^{\beta\gamma} - J^{\gamma\beta})$. The approximation of $D_\alpha = J^{\beta\gamma}$ can be used only when one is sure that the anisotropic symmetric elements of $\mathcal{J}$ are negligible. One example is that both DMI and Kitaev interactions are large in a $Cr(I,Br)_3$ Janus monolayer and similar systems (45). (*d*) Crystal symmetry analyses can reduce the amount of calculations. For example, the presence of an inversion center between site 1 and site 2 leads to vanishing DMI, and C_{4v} symmetry results in $J^{xx} = J^{yy}$. (*e*) The calculations of SIA matrix $\mathcal{A}$ also rely on four spin states, but with a formula that is different than Equation 7. See the appendix of Reference 44 for details.

Notably, it is very convenient to apply the four-state method to obtain the derivatives of exchange parameters with respect to atomic displacements (43) and strain (46). For this purpose, we take derivatives of the total energy expression,

$$\frac{\partial E}{\partial u_{k\alpha}} = \frac{\partial E_0}{\partial u_{k\alpha}} + \sum_{<i,j>} \frac{\partial J_{ij}}{\partial u_{k\alpha}} \mathbf{S}_i \cdot \mathbf{S}_j, \qquad 8.$$

where $u_{k\alpha}$ is the displacement of the kth atom along the α direction. Note that here we only consider isotropic exchange interactions for simplicity. Taking the four states used in Equation 7, one can easily have

$$\frac{\partial J_{12}}{\partial u_{k\alpha}} = \frac{1}{4S^2}\left(\frac{\partial E_1}{\partial u_{k\alpha}} - \frac{\partial E_2}{\partial u_{k\alpha}} - \frac{\partial E_3}{\partial u_{k\alpha}} + \frac{\partial E_4}{\partial u_{k\alpha}}\right), \qquad 9.$$

where $-\frac{\partial E_i}{\partial u_{k\alpha}}, (i = 1, \ldots, 4)$ is the force acting on the atom k along the α direction. The force can be computed using the Hellmann–Feynman theorem and is readily available in standard DFT schemes. Thus, the derivatives of $\frac{\partial J}{\partial u_{k\alpha}}$ can be immediately obtained from the forces from standard four-state calculations without any further computations. A similar procedure can be used to obtain the derivatives of exchange parameters with respect to strain (46). The second-order derivatives of exchange parameters with respect to atomic displacements in two-dimensional magnets were computed by combining the finite difference method and four-state method (47).

Although the four-state method was originally proposed to compute bilinear exchange interacting parameters, it was recently extended (39) to extract the coefficient B of fourth-order

biquadratic interaction $B(\mathbf{S}_i \cdot \mathbf{S}_j)^2$. In this case, another set of four states should be chosen. The four-state method can also be used to compute ME coupling strength, as we discuss below.

2.1.1.3. Symmetry-adapted cluster expansion method. The previous energy mapping methods can well handle Hamiltonians with only second-order interactions, whereas they may become inadequate when higher-order and many-body interactions are important. In such cases, the cluster expansion method is a good option (33, 37, 48, 49).

The symmetry-adapted cluster expansion method expresses spin interactions as polynomials made of spin components (S_α, $\alpha = x, y$, and z, and $S = 1$ are adopted here) that are invariant under all crystal symmetry operations, as well as the time-reversal symmetry (which excludes odd orders of interactions). Specifically, one can start with the Hamiltonian

$$\mathcal{H} = E_0 + \sum_N \mathcal{H}_N^{\text{spin}}, \qquad 10.$$

where E_0 is the nonmagnetic part, whereas $\mathcal{H}_N^{\text{spin}}$ is the Nth-order spin-related term. If we take the second- and the fourth-order interactions as examples, before applying symmetry, $\mathcal{H}_2^{\text{spin}}$ and $\mathcal{H}_4^{\text{spin}}$ can be written as

$$\begin{aligned} \mathcal{H}_2^{\text{spin}} &= \sum_{\langle i,j \rangle} \sum_{\alpha,\beta} c_{ij}^{\alpha\beta} S_{i\alpha} S_{j\beta}, \\ \mathcal{H}_4^{\text{spin}} &= \sum_{\langle i,j,k,l \rangle} \sum_{\alpha,\beta,\gamma,\delta} c_{ijkl}^{\alpha\beta\gamma\delta} S_{i\alpha} S_{j\beta} S_{k\gamma} S_{l\delta}, \end{aligned} \qquad 11.$$

where the sums run over all possible combinations of spin components; $\langle\ \rangle$ denotes a cluster of magnetic sites; i, j, k, and l are site indices that are chosen from the set of $\{1, 2, \ldots, M\}$ for an M-body cluster; and α, β, γ, and δ are Cartesian components of the spins. Let us now apply crystal symmetries to the above forms, which results in

$$\begin{aligned} \mathcal{H}_2^{\text{spin}} &= \sum_n J_n \sum_m c_{nm} S_{i^m\alpha^m} S_{j^m\beta^m}, \\ \mathcal{H}_4^{\text{spin}} &= \sum_n K_n \sum_m c_{nm} S_{i^m\alpha^m} S_{j^m\beta^m} S_{k^m\gamma^m} S_{l^m\delta^m}, \end{aligned} \qquad 12.$$

where the sums over n run through all invariants, and the sums over m collect all the terms within each invariant. Note that, besides biquadratic couplings and some specific fourth-order interactions, such methodology in principle covers all the possible forms of interactions. The interacting parameters J_n and K_n can be extracted by combining DFT calculations and a fitting procedure. If the number of parameters is small, one can adopt the simple linear least squares approach, which however fails in the case of complicated models. In this case, one can adopt a ML method (50) to find out the significant interacting terms of the Hamiltonian in which one not only tries to add terms but also tries to delete and substitute terms from the temporary model during searching for the important terms.

2.1.2. Perturbation-based methods. As an alternative to the total energy–based approaches, one can use analytical perturbation theory to express Heisenberg parameters in terms of Green's functions (51) or linear response functions (52, 53) that may be calculated directly from the magnetic ground state itself. The idea is to compare the change of energy between the Heisenberg model and DFT calculations under arbitrarily small variations of the spin configuration around the ground state. The key to these calculations is to use a converged charge density of a reference setup and then to estimate the change of the energy of a modified setup. So instead of performing full self-consistent DFT calculations for all setups, one needs to perform one self-consistent calculation for a single setup only. The success of these methods is due to the magnetic force

theorem (MFT), which states that the total energy variation δE coincides with the sum of one-particle energy changes for the occupied states at the fixed ground state potential in the first order on the perturbations of the charge and spin densities:

$$\delta E = \int_{-\infty}^{E_F} d\epsilon \epsilon \delta n(\epsilon), \qquad 13.$$

where E_F is the Fermi level and $n(\epsilon)$ is the electronic density of states at energy ϵ.

The perturbation-based method for computing exchange parameters was first proposed within the Green's function framework in the seminal work of Liechtenstein, Katsnelson, Antropov, and Gubanov (LKAG) (51, 54–58). Within tight-binding linear muffin-tin methods (59) the isotropic exchange interactions between magnetic moments can be calculated using the Green's function technique (60),

$$J_{ij} = \frac{1}{2\pi} \int_{-\infty}^{E_F} d\epsilon \mathrm{Im} \sum_{m,m',m'',m'''} \Delta_i^{m,m'} G_{ij\downarrow}^{m'm''} \Delta_j^{m'',m'''} G_{ji\uparrow}^{m'''m}, \qquad 14.$$

where m, m', m'', and m''' are magnetic quantum numbers; Δ_i is the local exchange splitting on site i; and G represents the intersite Green's function. The Green's function method allows determination of the Heisenberg magnetic interaction parameters from the ground-state solution of the system, regardless of whether it is ferromagnetic or antiferromagnetic. This method also allows access to a band-by-band decomposition of the different magnetic interactions. The method was also extended to correlated systems in References 61 and 62. By taking into account relativistic effects (SOC), the DMI (63) and the magnetic anisotropy can be calculated as well (61, 62). Higher-order terms in the Hamiltonian, like the four-spin interaction or the biquadratic term, were also calculated through this method (57, 64). Recently, He et al. (65) developed a Python package (`TB2J`) to compute the isotropic exchange, the anisotropic exchanges, and the DMI using Wannier functions or a linear combination of atomic orbitals DFT results with the Green's function technique.

It was shown (53) that the full microscopic exchange tensor may be expressed in terms of the static Kohn–Sham susceptibility tensor instead of the Green's function. Consider second-order change in the total energy related to the rotations of the magnetic moments appearing at sites $R + \tau$ and $R' + \tau'$ of the lattice (here R are the lattice translations and τ are the atoms in the basis): A linear response theory expresses the interatomic exchange constants in the form

$$J_{\tau R,\tau' R'}^{\alpha\beta} = \sum_{\mathbf{q}} \sum_{\mathbf{k}} \sum_{jj'} \frac{f_{\mathbf{k}j} - f_{\mathbf{k}+\mathbf{q}j'}}{\epsilon_{\mathbf{k}j} - \epsilon_{\mathbf{k}+\mathbf{q}j'}} \langle \psi_{\mathbf{k}j} | [\sigma \times \mathbf{B}_\tau]_\alpha | \psi_{\mathbf{k}+\mathbf{q}j'} \rangle \times \langle \psi_{\mathbf{k}+\mathbf{q}j'} | [\sigma \times \mathbf{B}_{\tau'}]_\beta | \psi_{\mathbf{k}j} \rangle e^{i\mathbf{q}(\mathbf{R}-\mathbf{R}')}. \qquad 15.$$

Here, σ is the Pauli matrix, $\mathbf{B}_\tau$ is the local magnetic field at atomic site τ, $\mathbf{k}$ and $\mathbf{q}$ are momentum, and f is the Fermi–Dirac distribution function. Within usual DFT, $\epsilon_{\mathbf{k}_j}$ and $\psi_{\mathbf{k}_j}$ are one-electron energy and the Kohn–Sham wave function, respectively. If correlation effects are taken into account (e.g., with the dynamical mean field theory) (66), the corresponding quasiparticle results should be adopted. This method was recently (67) implemented within a plane wave projector augmented wave (68) formalism. Compared to the total energy–based methods, the perturbation-based methods for computing exchange parameters are especially useful for dealing with low-energy excitations (such as magnon dispersion) but may not be accurate enough to describe the magnetic properties as temperature is increased up to the magnetic critical temperature.

2.2. Ferroelectrics

Ferroelectricity refers to the phenomenon that certain materials exhibit a spontaneous electric polarization, which can be reversed by the application of an external electric field. The polarization

is defined as the electric dipole moment in unit volume $\mathbf{P} = \mathbf{D}/\Omega$ (Ω denotes the volume) or on unit area $\mathbf{P} = \mathbf{D}/S$ (S denotes the lateral area), where the latter is generally used for two-dimensional ferroelectrics. Below, we introduce the applications of first-principles and related methods in ferroelectrics, including modern theory of electric polarization, finite electric field approach, and an effective Hamiltonian approach.

2.2.1. Modern theory of electric polarization. Although the calculation of electric dipole of a finite system is straightforward using $\mathbf{D} = \int \mathbf{r}\rho(\mathbf{r})d\mathbf{r}$ [$\rho(\mathbf{r})$ is the charge density], the calculation of electric polarization in crystalline solids is tricky due to the periodic boundary condition. This problem was resolved about three decades ago, when the modern theory of polarization was introduced (69, 70). The theory shows that the electric polarization in a crystalline solid is a lattice rather than a vector. The total polarization for a given crystalline structure is the sum of ionic and electronic contributions:

$$\mathbf{P} = \mathbf{P}_{\text{ion}} + \mathbf{P}_{\text{el}}. \qquad 16.$$

Here, the ionic contribution comes from the nucleus and core electrons and is given by $\mathbf{P}_{\text{ion}} = \frac{e}{\Omega}\sum_i Z_i \mathbf{r}_i$, where Ω is the volume of the unit cell, $\mathbf{r}_i$ is the ionic position in the unit cell and Z_i is the charge state of the ith ion. The electronic contribution is given as a Berry phase (71) term:

$$\mathbf{P}_{\text{el}} = -\frac{ie}{2\pi^3}\sum_{\sigma,n}^{occ}\int_{\text{BZ}} d^3\mathbf{k}\left\langle u^{\sigma}_{n\mathbf{k}} \middle| \frac{\partial u^{\sigma}_{n\mathbf{k}}}{\partial \mathbf{k}} \right\rangle, \qquad 17.$$

where $u^{\sigma}_{n\mathbf{k}} = e^{-i\mathbf{k}\mathbf{r}}\Psi^{\sigma}_{n\mathbf{k}}(\mathbf{r})$ is the periodic part of the Bloch function.

2.2.2. Finite electric field approach. Many physical properties (such as dielectric constant, Born effective charge, piezoelectric coefficient) of ferroelectrics can be expressed as derivatives of the total energy of the solids with respect to a macroscopic field $\boldsymbol{\varepsilon}$ at $\boldsymbol{\varepsilon} = 0$, which can be computed with density functional perturbation theory (72, 73). Although for many applications such perturbation approaches are adequate, in some cases (e.g., switching ferroelectric domains) it is essential to perform calculations directly at finite fields. Souza et al. (74) and Umari & Pasquarello (75) proposed a first-principles approach based on the minimization of an electric enthalpy functional $\mathcal{F}$ with respect to Bloch-like functions under a given electric field $\boldsymbol{\varepsilon}$, where $\mathcal{F}$ is composed of the usual Kohn–Sham energy and a field coupling term:

$$\mathcal{F}(\boldsymbol{\varepsilon}, \nu) = E_{\text{KS}}(\nu) - \Omega\mathbf{P}(\nu)\cdot\boldsymbol{\varepsilon}, \qquad 18.$$

where ν represents the internal (ionic and electronic) coordinates. The fixed electric field approach is used to treat insulators under closed-circuit boundary conditions with a fixed voltage. To impose the open-circuit electrical boundary conditions, a finite electric displacement approach was proposed by Stengel et al. (76). In this technique, they introduced a new functional,

$$U(\mathbf{D}, \nu) = E_{\text{KS}}(\nu) + \frac{\Omega}{2\epsilon_0}[\mathbf{D} - \mathbf{P}(\nu)]^2, \qquad 19.$$

where ϵ_0 is the vacuum permittivity. To obtain the state under a given electric displacement $\mathbf{D}$, the functional is minimized with respect to the electronic and/or ionic coordinates ν.

2.2.3. Effective Hamiltonian approach. Part of the fascination of ferroelectrics is related to the fact that they undergo temperature-driven structural phase transitions and various functional properties (e.g., dielectric and piezoelectric properties) are strongly temperature dependent, being especially large or even divergent near the phase transition temperatures. The most straightforward way to account for the effects of temperature would be to perform ab initio DFT molecular

dynamics (MD) simulations. However, this approach is so computationally intensive that currently it is restricted to relatively small systems and timescales. For finite-temperature investigations, the first-principles effective Hamiltonian approach was proposed (77). Besides the high efficiency, the effective Hamiltonian approach is very helpful in clarifying the microscopic mechanisms responsible for ferroelectricity. In this approach, one defines a reduced number of degrees of freedom per unit cell and constructs a model Hamiltonian $\mathcal{H}_{\mathrm{FE}}$ with the internal energy written as

$$E_{\mathrm{FE}} = E^{\mathrm{self}}(\mathbf{u}_i) + E^{\mathrm{dpl}}(\mathbf{u}_i) + E^{\mathrm{short}}(\mathbf{u}_i) + E^{\mathrm{elas}}(\eta_i) + E^{\mathrm{int}}(\eta_i, \mathbf{u}_i), \qquad 20.$$

where $\mathbf{u}_i$ is the local soft-mode in unit cell i, η is the total strain tensor, E^{self} is the local mode self-energy, E^{dpl} characterizes the long-range interactions between local modes, E^{short} mimics the short-range interactions between local modes in the form, E^{elas} is the elastic energy, and E^{int} represents the interactions between local modes and strains. By fitting the DFT results, one arrives at an effective Hamiltonian model, typically containing 10–20 parameters, that can be subjected to Monte Carlo (MC) or MD simulations in order to determine the finite-temperature properties of the material. Different from the usual effective Hamiltonian approach, which only treats a subset of relevant degrees of freedom, Ìniguez and his coworkers proposed (78) to create models that describe the energetics of a material by Taylor expanding the potential energy surface around a suitably chosen reference structure as a function of all the atomic degrees of freedom.

2.3. Multiferroics

Multiferroicity refers to the coexistence of two or more ferroic orders in one material. Here, we focus on the ME multiferroics, which possess both magnetism and ferroelectricity. The main goal is to reveal the mechanisms of ME couplings and to enhance such couplings. In the following, we introduce the first-principles related methods that deal with spin–lattice interactions, spin-induced ferroelectricity and linear ME effect. Such methods are used to study ME couplings or to build the models with coupled spin and structural freedoms.

2.3.1. Spin–Lattice Hamiltonians. One of the important ME couplings is the spin-lattice interaction, which involves the couplings of spin moments with atomic displacements and strains. Here, we introduce two methods to obtain spin-lattice Hamiltonians, the general effective Hamiltonian approach and the machine learning potentials method.

2.3.1.1. General effective Hamiltonian approach. The effective Hamiltonian approach initially proposed for ferroelectrics was generalized to multiferroics recently. For instance, in the perovskite multiferroic $BiFeO_3$, the magnetic degree of freedom (i.e., the magnetic moment on the Fe sites) was incorporated (79) in the effective Hamiltonian to describe the magnetic interactions and spin–lattice interactions. The symmetry-adapted cluster expansion method was further extended to deal with multiferroics with any symmetry (48). To describe the interplay between different degrees of freedom in multiferroics, in general, the effective Hamiltonian $\mathcal{H}_{\mathrm{sl}}$ should consist of three parts: the magnetic effective Hamiltonian $\mathcal{H}_{\mathrm{spin}}$, the effective Hamiltonian for ferroelectrics $\mathcal{H}_{\mathrm{FE}}$, and a spin–lattice coupling term $\mathcal{H}_c(\mathbf{S}_i, \mathbf{u}_j, \eta)$, which describes the couplings between spin and structural modes (including the local soft mode and other antiferroelectric degrees of freedom $\mathbf{u}_j$ and strain η). Similar to the spin Hamiltonian case, one adopts the group theory to find out the Hamiltonian form of the lattice part $\mathcal{H}_{\mathrm{FE}}$ and the spin–lattice coupling part $\mathcal{H}_{\mathrm{c}}$. Then the parameters of the full Hamiltonian can be determined by combining a parameter selection procedure (e.g., the so-called ML approaches for constructing effective Hamiltonians) (50) and DFT calculations. In order to obtain the dynamic behavior of the multiferroic system, one needs to perform spin–lattice dynamics simulations (48, 80) with the general effective Hamiltonians. This general

effective Hamiltonian approach and the corresponding MC and spin–lattice dynamics methods were implemented in the property analysis and simulation package (PASP) for materials (48).

2.3.1.2. Machine learning potentials. Machine learning interatomic potentials (MLIPs) have become a significant asset to the field of computational condensed matter physics by providing a powerful tool for accurately simulating materials (81–84). MLIP models are trained using a data set of atomic configurations and their respective total energies or forces, which allows them to learn the underlying potential energy surface of a system. By using this learned potential energy surface, it is possible to investigate behaviors under different conditions, such as temperature, pressure, or deformation for studying large, complex materials systems over extended periods. MLIPs are advantageous over the effective Hamiltonian method in capturing complex potential functions for structures with large perturbations (85). Graph neural networks (GNNs) and equivariant neural networks (ENNs) are recent developments in MLIPs that allow for accurate predictions of the properties of complex systems with millions of atoms with near-first-principles accuracy (86, 87). While message passing neural networks perform exceptionally well in training potential, their parallelism limits their use for large-scale simulations. Strictly local equivariant deep neural networks, such as Allegro (88), address this challenge and enable accurate and scalable predictions of complex systems.

Despite making significant progress in expanding the range of systems and physical phenomena that can be studied using MLIPs, their inability to account for various spin configurations and their associated magnetic interactions remain a drawback (89, 90). Ideal MLIP models for magnetic materials have to meet several requirements, including the abilities to describe both collinear and noncollinear magnetic moment states; take into account the effect of SOC if needed; and adhere to the symmetry principles of inversion, translation, and rotation, as well as time-reversal symmetry, which is also referred to as spin inversion symmetry (91). Most MLIPs are designed without the freedom degrees of atomic magnetic moments, making it challenging for MLIP models to describe the spin–lattice coupling in magnetic materials.

Several MLIPs considering magnetic moments based on atomic descriptors have been developed (89, 92–96). Novikov et al. (96) proposed magnetic moment tensor potentials (mMTPs), which adds the contributions of collinear magnetic moments on moment tensor potentials (MTPs) to include collinear magnetic degrees of freedom in MLIPs. The mMTP was adopted to perform phonon calculations and MD simulations for the prototype magnetic system bcc (body-centered cubic) iron. However, the mMTP method does not explicitly consider spin-inversion symmetry. Additionally, Eckhoff & Behler (89) developed magnetic high-dimensional neural network potentials (mHDNNPs), which modify the atomic cluster surface functionals (ACSFs) to spin-dependent ACSFs (sACSFs). Like mMTPs, mHDNNPs can only deal with collinear magnetic moments, preventing their usage in studying noncollinear magnetic states such as spirals, skyrmions, and bimerons. Meanwhile, Yu et al. (90) developed spin descriptors to construct the complex neural network spin Hamiltonian. Furthermore, Nikolov et al. (95) proposed magnetoelastic ML-IAP, which use the spectral neighbor analysis potential (SNAP) (97) and an effective spin–lattice Hamiltonian considering Heisenberg and biquadratic terms. Chapman & Ma (92) developed a machine-learned spin–lattice interatomic potential (MSLP) for iron with the nonmagnetic term, the Heisenberg–Landau term, and a remaining neural network term using the local atomic and magnetic descriptors. Domina et al. (93) introduced an invariant power spectrum representation for vectorial fields and developed spin SNAP based on the SNAP descriptor (97). Note that all these descriptors-based magnetic MLIPs do not take into account the SOC.

Because of the high flexibility and accuracy provided by GNNs, magnetic MLIPs based on GNNs were developed very recently (91, 98). Yu et al. have proposed SpinGNN (98) and SpinGNN++ (91), which integrate the spin configuration into the GNN framework shown in

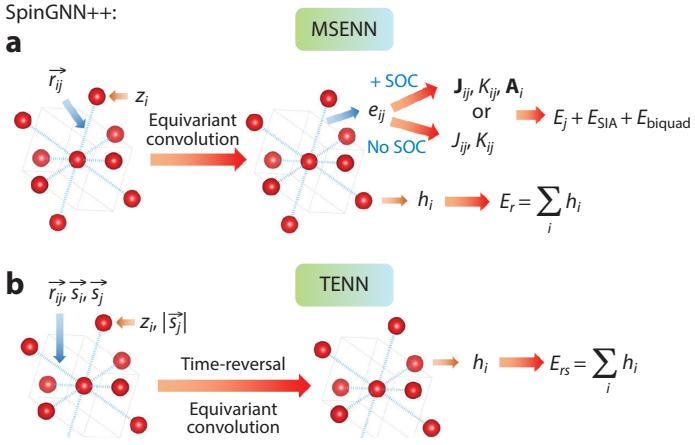

Figure 4

Illustration of building a general neural network potential for multiferroics with a SpinGNN++ framework. It includes the MSENN and TENN. (*a*) Utilization of the updated edge feature of an ENN to predict the *J* matrix, SIA matrix, and the biquadratic coefficient to build a magnetic potential. (*b*) Adoption of the TENN to build a high-order general magnetic potential, where the node and edge are initialized with the spin vector. Abbreviations: ENN, equivariant neural network; GNN, graph neural network; MSENN, multitask spin equivariant neural network; SIA, single-ion anisotropy; SOC, spin–orbit coupling; TENN, time-reversal equivariant neural network.

Figure 4. They constructed Spin-DimeNet++ and Spin-Allegro based on SpinGNN, which successfully describes several effective spin–lattice Hamiltonian models and the multiferroic $BiFeO_3$. Additionally, they extended ENN to time-reversal ENN (TENN), which incorporates time-reversal symmetry (91) besides the translation, inversion, and rotation symmetries considered in the usual ENN. With TENN, Yu et al. built a general spin–lattice model for magnetic materials that meets the requirements of an ideal magnetic neural network potential. This model of a multiferroic contains three parts:

$$E_{\mathrm{MF}}(\mathbf{S},\mathbf{u}) = E_0^{\mathrm{NN}}(\mathbf{u}) + \sum_{<i,j>} \mathbf{S}_i \cdot \mathcal{J}_{ij}^{\mathrm{NN}}(\mathbf{u}) \cdot \mathbf{S}_j + \sum_{<i>} \mathbf{S}_i \cdot \mathcal{A}_i^{\mathrm{NN}}(\mathbf{u}) \cdot \mathbf{S}_i + \sum_{<i,j>} K_{ij}(\mathbf{u})(\mathbf{S_i} \cdot \mathbf{S_j})^2 + \mathbf{E}_{\mathrm{high\text{-}order}}^{\mathrm{NN}}(\mathbf{S},\mathbf{u}), \quad 21.$$

where the first part $E_0^{NN}(\mathbf{u})$ ($\mathbf{u}$ represents the atomic structural information) is the contribution unrelated to spins, the second and third parts are the bilinear spin interaction, the fourth part is the biquadratic term, and the fifth part is the high-order spin–lattice interacting term, respectively. This model can serve as a general potential for multiferroic materials and can be used for performing large-scale spin–lattice dynamics and MC simulations.

2.3.2. Unified model for spin-induced ferroelectricity. From the perspective of symmetry, ferroelectricity breaks spatial inversion symmetry. If the crystal structure itself satisfies spatial inversion symmetry, but its magnetic structure does not, then the magnetic order may induce ferroelectric polarization. Since 2005, Nagaosa, Dagotto, and others have proposed several microscopic models (99–103) that partially explain the phenomenon of magnetic order–induced ferroelectricity. For example, Nagaosa and colleagues (101) proposed a spin current model to explain the ferroelectricity induced by the noncollinear spiral order: $\mathbf{P} \propto \sum_{i,j} \mathbf{e}_{ij} \times (\mathbf{S}_i \times \mathbf{S}_j)$, where $\mathbf{e}_{ij}$ is the distance vector from spin i to spin j. Unfortunately, as these models were derived for special cases, they are not general and have some limitations.

Since 2011, Xiang and colleagues have proposed a unified polarization model for describing spin-order-induced ferroelectricity (104–107). The model considers that the spin-order-induced electric polarization contains two parts:

$$\mathbf{P}_t = \mathbf{P}_e(\mathbf{S}_i, \mathbf{u}_j = 0, \eta_l = 0) + \mathbf{P}_{\text{ion-latt}}(\mathbf{u}_j(\mathbf{S}), \eta_l(\mathbf{S})), \quad 22.$$

where $\mathbf{S}_i$ represents the spin of the magnetic ion, $\mathbf{u}_j$ represents the displacement of the ion relative to the reference structure (generally a high-temperature centrosymmetric structure), and η_l represents the l component of the strain relative to the reference structure. The pure electronic part P_e describes the polarization induced by the charge redistribution caused by spin ordering, whereas the ion–lattice part $\mathbf{P}_{ion-latt}$ describes the polarization induced by ion displacement and lattice distortion caused by spin–lattice coupling. As the electric polarization is invariant with respect to the time-reversal symmetry, the pure electronic part $\mathbf{P}_e$ can be expressed as an even-order function (usually second order is enough) of the spins

$$\mathbf{P}_e = \sum_{i,\alpha,\beta} \mathbf{P}_i^{\alpha,\beta} S_{i,\alpha} S_{i,\beta} + \sum_{i,j,\alpha,\beta} \mathbf{P}_{ij}^{\alpha,\beta} S_{i,\alpha} S_{j,\beta}, \quad 23.$$

where the first term is the intrasite term related to a single spin, determined by the polarization parameter matrix $\mathbf{P}_i^{\alpha,\beta}$, and the second term is the intersite term related to spin pairs determined by the polarization parameter matrix $\mathbf{P}_{ij}^{\alpha,\beta}$. To obtain the ion–lattice contribution to the polarization, it is necessary to calculate the polar ion displacement and lattice distortion caused by spin ordering. Given the spin–lattice effective Hamiltonian H_{sl}, one can obtain the ion displacement $\mathbf{u}_j(\mathbf{S})$ and strain $\eta_l(\mathbf{S})$ induced by the spin order by solving

$$\frac{\partial \mathcal{H}_{\text{sl}}(\mathbf{S}_i, \mathbf{u}_j, \eta_l)}{\partial \mathbf{u}_j} = 0, \quad 24.$$

$$\frac{\partial \mathcal{H}_{\text{sl}}(\mathbf{S}_i, \mathbf{u}_j, \eta_l)}{\partial \eta_l} = 0. \quad 25.$$

Then, using the Born effective charge $Z_{j,\alpha\beta}$ and the piezoelectric coefficient $e_{\alpha,l}$, the ion–lattice displacement contribution to polarization can be obtained:

$$P_{\text{ion-latt},\alpha} = \sum_{j,\beta} Z_{j,\alpha\beta} u_{j\beta}(\mathbf{S}) + \sum_{l} e_{\alpha,l} \eta_l(\mathbf{S}). \quad 26.$$

All parameters involved in the unified model can be obtained by combining DFT calculations and four-state method.

2.3.3. Linear magnetoelectric effects. In insulating materials in which both spatial inversion and time-reversal symmetries are broken, there exists a linear ME effect (108); i.e., a magnetic field $\mathbf{B}$ can induce a first-order electric polarization $\mathbf{P}$, and conversely an electric field $\mathbf{E}$ can induce a first-order magnetization $\mathbf{M}$. Note that all electromagnetic multiferroics display the linear ME effects, but a material (e.g., Cr_2O_3) that displays the linear ME effect may not be a multiferroic. This linear ME effect is described by the susceptibility tensor,

$$\alpha_{ij}^{\text{ME}} = \frac{\partial P_i}{\partial B_j}\Big|_{\mathbf{B}=0} = \frac{\partial M_j}{\partial \varepsilon_i}\Big|_{\varepsilon=0}, \quad 27.$$

where indices label spatial directions. The linear ME effect is caused by, for example, an electric field changing the angles and distances, and hence the magnetic exchange interactions, between magnetic ions, or a magnetic field reorienting spin magnetic moments, causing a change in the

electronic charge density via the SOC. This ME tensor can be divided into a frozen-ion contribution that occurs even when the ionic coordinates are fixed, and a lattice-mediated contribution corresponding to the remainder. Each of these two contributions can be decomposed further according to whether the magnetic interaction is associated with spins or orbital currents, giving four contributions to α^{ME} in total.

Let us first focus on the linear ME effect related to electron spins. The first DFT-based study (109) extracted the ionic spin contribution to α^{ME}, by calculating the change in spin canting caused by freezing in an electric field–induced polar distortion of the ions without additionally explicitly coupling ε to the electrons, and the lattice contribution can be written as a product of the Born effective charge, the force-constant inverse, and the dynamical magnetic charge (110). For the electronic spin component of α^{ME} (111), one can calculate the electric polarization induced by an applied Zeeman $\mathbf{H}$ field coupled only to the spin component of the magnetization. Here, the electronic spin response is obtained by clamping the ions during the calculation; relaxing the ionic positions in response to the $\mathbf{H}$ field yields the sum of the ionic and electronic spin components. If the lattice constant is also allowed to relax, an additional strain-mediated ionic response can be extracted. It was realized recently (112) that the unified model for spin-induced ferroelectricity can be adopted to compute both electronic and ionic spin contributions to α^{ME}. First, one can compute the ionic displacement $\mathbf{u}_i$ and strain η_j induced by a small external electric field with a method similar to that adopted by Ìniguez (109). Then, one can estimate the change of the spin interactions due to the applied external electric field. Finally, the change of spin magnetization can be obtained by finding the magnetic ground state of the system with the modified spin interactions. The key quantity in this approach is the total derivative of the spin interaction strength of a given spin pair with respect to ε,

$$\frac{\mathrm{d}J^{\alpha\beta}}{\mathrm{d}\varepsilon} = \frac{\partial J^{\alpha\beta}}{\partial \varepsilon} + \sum_i \frac{\partial J^{\alpha\beta}}{\partial \mathbf{u}_i} \cdot \frac{\partial \mathbf{u}_i}{\partial \varepsilon} + \sum_j \frac{\partial J^{\alpha\beta}}{\partial \eta_j} \frac{\partial \eta_j}{\partial \varepsilon}, \qquad 28.$$

where the first part can be regarded as the electron contribution; $\frac{\partial J^{\alpha\beta}}{\partial \varepsilon}$ and the other two parts related to $\frac{\partial J^{\alpha\beta}}{\partial \mathbf{u}_i}$ and $\frac{\partial J^{\alpha\beta}}{\partial \eta_j}$ are lattice contributions. Note that all the three types of partial derivatives of $J^{\alpha,\beta}$ can be computed with the four-state method. The advantage of this approach to α^{ME} is that no external field is required, and the individual contribution to the spin contribution of α^{ME} from each spin pair can be easily identified. An equivalent way to compute α^{ME} is to find the new magnetic configuration under a Zeeman magnetic field and then compute the induced electric polarization with the unified model. In principle, the nonlinear ME effect can be treated in the same way.

Usually, the spin contribution to α^{ME} will dominate with respect to the orbital one, because orbital moments are usually strongly quenched by crystal fields. Under certain circumstances, the orbital contribution might become important. For example, Z_2-odd topological insulators may display a large, quantized orbital ME response. It was established (113, 114) that the orbital ME response of a generic insulator at zero field comprises three contributions that were denoted as local circulation, itinerant circulation, and Chern–Simons. Among them, the former two (Kubo) terms contribute to α^{ME} in conventional MEs, whereas the Chern–Simons term is responsible for the topological ME effect. Full ME response of Cr_2O_3 was computed from first-principles (115), showing that in the case of the longitudinal response, orbital contributions to α^{ME} dominate over spin contributions. Scaramucci et al. (116) proposed an alternative way for computing ionic orbital contribution to α^{ME} by considering the dependence of orbital magnetic moments on the polar distortions induced by an applied electric field.

3. RECENT PROGRESS IN MULTIFERROICS

Although multiferroics are of great importance for both fundamental study and practical applications, they are known to be rare in conventional materials. This is due to the fact that the partially occupied *d* orbitals of transition metal ions associated with magnetism reduce the tendency for off-center ferroelectric distortion (15). The emergence of two-dimensional materials, which exhibit diverse properties and novel mechanisms, provides a new avenue for realizing multiferroicity. Below, we summarize recent developments of two-dimensional multiferroics, where first-principles approaches play an important role.

3.1. Type-I Multiferroics

Type-I multiferroicity indicates that the ferroelectricity and magnetism of the system arise from different origins. For example, in $BiFeO_3$, the $6s^2$ lone pair of bismuth contributes to the polarization, whereas the $3d$ electrons of iron lead to magnetism. Here, we introduce recently proposed and observed type-I multiferroics.

3.1.1. VOI_2 type. VOI_2 belongs to the family of van der Waals layered multiferroics VOX_2 (X = Cl, Br, I) (117–119). As shown in **Figure 5*a***, VOX_2 are made up of VO_2X_4 octahedra. Neighboring V atoms share a corner O along one direction and an edge X_2 along the other direction. The paraelectric phase crystalizes in a Pmmm space group, whereas the ferroelectric phase condenses to Pmm2 symmetry. The in-plane polarization arises from the off-center displacement of V atom toward O atom. The magnetism originates from V^{4+} ($3d^1$) cation. It is predicted that $VOCl_2$ and $VOBr_2$ exhibit antiferromagnetism. Such properties indicate that the VOX_2 compounds belong to type-II multiferroics, which is similar to many perovskites. Interestingly, the emergence of ferroelectricity in VOX_2 is against the d^0 rule as V^{4+} exhibits $3d^1$ configuration. Such novel behavior is explained by the fact that the occupied *d* orbital of V^{4+} lies in the VX_4 plane and thus does not hinder V^{4+} moving toward oxygen.

Particularly, VOI_2 was predicted to possess ferromagnetic couplings (124), and strong DMI was proposed to exist in its ferroelectric phase (120). The DMI, which leads to spin spirals and bimeron state, originates from the off-center displacement of the V atom and the strong SOC of I atoms. Furthermore, the sign of the DMI changes when the polarization switches directions, which further leads to a reversal of the topological charge of the bimeron (120, 125). Such electromagnetic coupling between polarization and magnetic topological charge, mediated by DMI, implies a new route toward electric control of magnetism.

3.1.2. $CuCrS_2$ type. Bulk $CuCrX_2$ (X = S, Se) crystalize in an R3m space group. Although they are not van der Waals layered, first-principles calculations indicate that two-dimensionally formed $CuCrX_2$ are multiferroics (121). As shown in **Figure 5*b***, each two-dimensional multiferroic unit contains two layers of CrX_2 and one layer of intercalating Cu. In the ferroelectric phase, the Cu atom is vertically aligned with the Cr atom in the upper layer and the X atom in the lower layer, where the asymmetry leads to the polarization. The polarization is reversed if Cu is vertically aligned with the X atom in the upper layer and the Cr in the lower layer. The intrinsic magnetism is associated with the CrX_2 layers, making $CuCrS_2$ and $CuCrSe_2$ type-I multiferroics. Notably, two-dimensional $AgCrS_2$, which is isostructured with $CuCrX_2$, is recently prepared from its bulk form (126). Furthermore, reversible DMI, as well as topological defects, is predicted in two-dimensional $Ag(CrSe_2)_2$ (127), the mechanism of which is in line with that of VOI_2.

3.1.3. Free-standing perovskite thin films. In 2018, Lu et al. (128) theoretically investigated the properties of free-standing two-dimensional ferroelectric perovskite oxide thin films. They

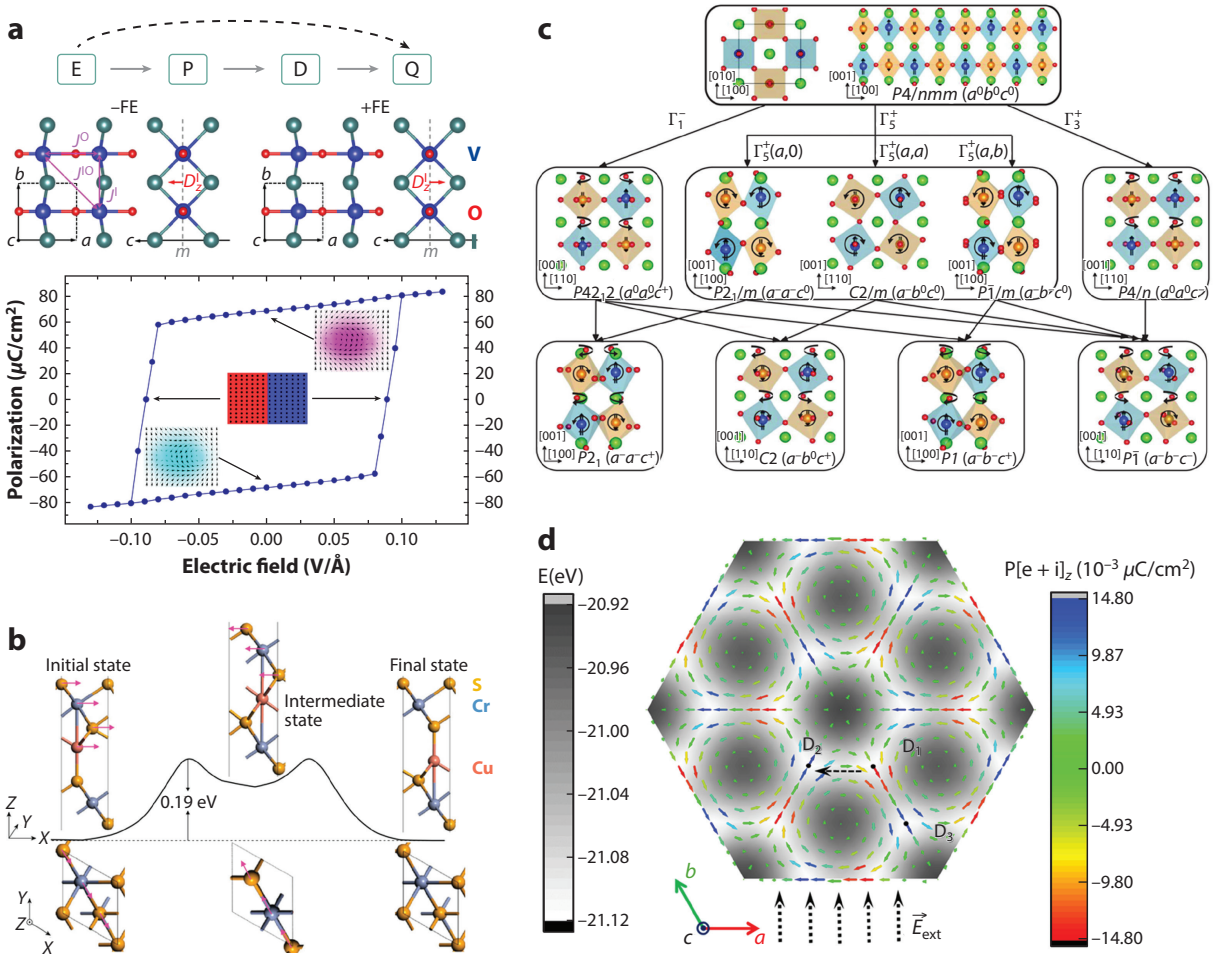

Figure 5

A collection of two-dimensional type-I multiferroics. (*a*) The EPDQ mechanism, which indicates that applying electric field (E) can reverse the polarization (P) and the DMI (D) vector, and further changes the sign of the magnetic topological charge (Q), is proposed to be realized in VOI2. The blue, red, and green balls represent V, O, and I atoms, respectively. (*b*) The transition path from positive to negative polarization states of $CuCrS_2$. (*c*) The possible octahedra rotation modes in B-site-ordered double-perovskite bilayer. (*d*) The energy and polarization distribution of 60°-rotated bilayer CrI_3. Panel *a* adapted from Reference 120. Panel *b* adapted from Reference 121. Panel *c* adapted from Reference 122. Panel *d* adapted from Reference 123. Abbreviation: DMI, Dzyaloshinskii–Moriya interaction.

found that there exist three kinds of in-plane ferroelectric states that originate from different microscopic mechanisms: (*a*) a proper ferroelectric polarization due to the second-order Jahn–Teller effect related to the B ion with empty *d*-orbitals; (*b*) a polarization induced by the surface effect; and (*c*) a hybrid improper ferroelectric state induced by the trilinear coupling between two rotational modes and the A-site displacement. Interestingly, the latter two ferroelectric mechanisms are compatible with magnetism because their stability does not depend on the occupation state of the *d*-orbitals of the B ion. These two novel two-dimensional ferroelectric mechanisms provide new avenues to design two-dimensional multiferroics, as they demonstrated in Sr-V-O and Ca-Fe-O thin films. Subsequently, Zhang et al. (122) theoretically examined ferromagnetic

B-site-ordered double-perovskite bilayers and found two coupling mechanisms between polarization and magnetization that enable the reversal of the in-plane magnetization by ferroelectric switching (see **Figure 5*c***). The spin-induced ferroelectricity and its coexistence and coupling with ferromagnetism or ferrimagnetism were predicted in even-layer double-perovskite systems (129). The coexistence of and coupling between ferroelectricity and ferromagnetism were also demonstrated in designed A-site-ordered perovskite oxide monolayers (130). On the experimental side, Ji et al. (131) synthesized freestanding crystalline perovskite oxide thin films down to the monolayer limit in 2019. They further found that freestanding $BiFeO_3$ films exhibit unexpected giant tetragonality and polarization when approaching the two-dimensional limit.

3.1.4. Bilayer CrI_3 and VS_2. Recently, the emergence of two-dimensional magnets and sliding ferroelectricity has opened up a new approach toward multiferroicity. Sliding ferroelectricity was initially proposed in bilayer BN, where different stackings can result in opposite polarizations (132). Recent work based on group theory analysis covers all symmetries and provides all possible cases for stacking ferroelectricity (123). Therefore, it is straightforward to construct bilayer multiferroics with two-dimensional magnets. Due to the different sources of magnetism and ferroelectricity, such bilayer systems are considered to be type-I multiferroics. One example is bilayer CrI_3, for which the two monolayers rotate 60° with respect to each other (77, 133). Interestingly, group theory predicts that the 60°-rotated bilayer CrI_3 has both in-plane and out-of-plane components of polarization, which enables tuning of ferroelectricity and magnetism via electric fields (see **Figure 5*d***). Another example is the bilayer VS_2 (134), which exhibits ferroelectricity and antiferromagnetism, as well as ferrovalley (135).

3.2. Type-II Multiferroic

Type-II multiferroicity refers to the phenomenon that ferroelectricity is induced by magnetism, where the latter plays the role of breaking inversion symmetry. Type-II multiferroicity usually leads to strong ME coupling.

3.2.1. NiI_2 Type. Recent experiments with optical second-harmonic generation technique demonstrate that a few layers and even a monolayer of NiI_2 are possible two-dimensional multiferroics (136, 137).

The bulk form of NiI_2 has been known as a type-II multiferroic since 2013 (138). It is a van der Waals layered material, with each layer of NiI_2 being made of a triangular lattice of Ni^{2+} ($3d^8$, $S = 1$) ions (see **Figure 6*a***). The magnetic ground state of bulk NiI_2 possesses a helical structure propagating along $\mathbf{q} \approx (0.138, 0, 1.457)$, which corresponds to the equivalent $\langle 1\bar{1}0\rangle$ directions. Notably, the spins rotate in a plane that forms an angle of 55° with the out-of-plane direction (141). Such spin pattern breaks the crystal inversion symmetry and induces an in-plane polarization along $\langle 110\rangle$ directions, which is perpendicular to the magnetic propagation direction, yielding a type-II multiferroic.

The helical magnetic structure of NiI_2 results from the competition of Heisenberg interactions (142), where competition among the first-, second-, and third-nearest neighbors determines the propagation direction. It was believed that the $\langle 1\bar{1}0\rangle$ is due to competing ferromagnetic J_1 and antiferromagnetic J_2 (136, 142). However, this contradicts with models extracted from DFT, which predict $\langle 110\rangle$ propagation as J_2 is usually negligibly small (34, 143–145). Furthermore, the tight-binding model predicts Kitaev interaction in NiI_2, and this was soon confirmed by DFT calculations with the four-state method (144). It is further demonstrated that the Kitaev interaction not only prefers the $\langle 1\bar{1}0\rangle$ propagation but also dominantly determines the 55° canting of the spin rotation plane (33).

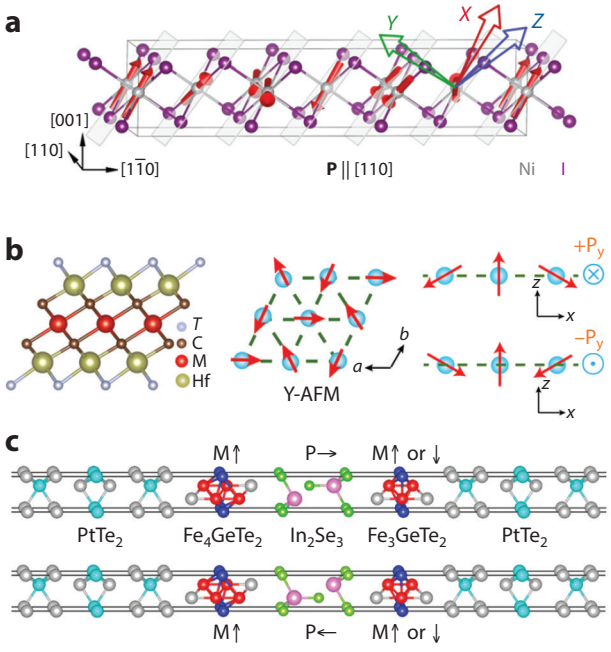

Figure 6

Examples of two-dimensional type-II multiferroics (*a*,*b*) and multiferroic heterostructures (*c*). (*a*) The canted proper screw spin state shown in a single layer of NiI_2. The lightly shaded planes indicate the rotation plane of spins, and the Kitaev basis of {*XYZ*} is shown with red, green, and blue arrows. (*b*) Multiferroic MXene of $Hf_2VC_2F_2$, the structure, noncollinear magnetic state, and induced polarization. (*c*) The multiferroic heterostructure of $Fe_4GeTe_2/In_2Se_3/Fe_3GeTe_2$. Panel *a* adapted with permission from Reference 33. Panel *b* adapted from Reference 139. Panel *c* adapted from Reference 140. Abbreviation: Y-AFM, Y-type antiferromagnetism.

The triangular lattice and competing $J_1 - J_2 - J_3$ mechanism, as well as the novel Kitaev interaction, represents many similar multiferroics. Examples include $NiBr_2$, MnI_2, and CoI_2, where polarizations are induced by different helical spin textures (138, 146, 147). Such compounds are all van der Waals layered and, thus, in principle can be made into two-dimensional multiferroics.

3.2.2. $Hf_2VC_2F_2$. The MXenes come into play as a brand new type of multiferroics. MXenes can be easily exfoliated from their three-dimensional parent compounds called MAX, which show good flexibility in their chemical composition. Recently, the MXene of $Hf_2VC_2F_2$ is predicted by first-principles calculations to be a type-II multiferroic, where ferroelectricity originates directly from its magnetism (139). The noncollinear 120° Y-type spin order generates a polarization perpendicular to the spin helical plane. Remarkably, the multiferroic transition is estimated to occur above room temperature (see **Figure 6*b***). Considering the diversity of MXenes, it is legitimate to expect more multiferroics out of this type.

3.3. Multiferroic Heterostructures

Besides the aforementioned homostructures, heterostructures made of 2D ferromagnets and ferroelectrics lead to more possibilities of multiferroics. As an established 2D ferroelectric, In_2Se_3 is a popular choice for constructing such heterostructures. For example, as shown in **Figure 6*c***, multiferroic tunnel junctions of $Fe_mGeTe_2/In_2Se_3/Fe_nGeTe_2$ (m, n = 3, 4, 5; $m \neq n$) exhibit

multiple nonvolatile resistance states associated with different polarization orientations of the ferroelectric In_2Se_3 layers and magnetization alignment of the two ferromagnetic Fe_nGeTe_2 layers (140). The bilayer made of $CrGeTe_3$ and In_2Se_3 is predicted to exhibit in-plane versus out-of-plane anisotropy in its magnetism at different polarization states. In another bilayer made of $MnSTe/In_2Se_3$, the creation and annihilation of the topological magnetic phase can be achieved when the polarization is switched. MXenes with polar structures, such as Ti_2NC_2 or Sc_2CO_2, are also used as the ferroelectric layer. For example, a trilayer made of monolayer Sc_2CO_2 and bilayer CrI_3 is predicted to exhibit ferromagnetism versus antiferromagnetism when the polarization is switched (148).

4. CONCLUSION AND PERSPECTIVE

We have conducted a review of first-principles and first-principles-based techniques and their applications in the areas of magnets, ferroelectrics, and multiferroics. These approaches offer computational means to determine various ferroic properties such as the amplitudes and signs of magnetic interactions, electric polarization values, and ME coupling forms and strengths. Additionally, these methods facilitate the construction of models incorporating spin and lattice degrees of freedom, allowing for extensive MC and dynamic simulations. Our review also highlights the recent advancements in the field of two-dimensional multiferroics, wherein first-principles methods play a crucial role.

Despite the tremendous progress made in the field of multiferroics, there are still two major challenges to be overcome before the full potential of these materials can be realized. One challenge is to identify and develop materials with strong coupling between their magnetic and ferroelectric properties at room temperature. Another challenge is the development of robust, efficient, and high-speed methods for controlling and manipulating the magnetic and ferroelectric domains of these materials. To this end, new powerful first-principles-based approaches have to be developed. In order to accelerate the discovery of new multiferroic materials, one promising way is to perform screenings that combine the use of a materials database and a high-throughput approach. Another way is to use ML models trained with DFT results to predict the properties of a material much more efficiently or to intentionally design high-performance multiferroics. To investigate the dynamics of multiferroics, the development of first-principles approaches that can simulate the time-resolved behaviors, such as a more reliable and more efficient real-time time-dependent DFT (149), could be valuable. As defects can create local electric dipoles or modify the magnetic interactions and thus affect the switching of ferroelectric or magnetic domains, it is crucial to examine the effects of defects (such as vacancies, interstitials, and impurities) on the properties of multiferroics as well. However, treating defects in multiferroics with current first-principles approaches is difficult due to the large unit cells needed and the fact that the electric polarization of a defect system may be ill defined within the Berry phase theory.

DISCLOSURE STATEMENT

The authors are not aware of any affiliations, memberships, funding, or financial holdings that might be perceived as affecting the objectivity of this review.

ACKNOWLEDGMENTS

We acknowledge financial support from the National Key R&D Program of China (grant 2022YFA1402901 and grant 2022YFA1402903). H.X. also acknowledges support from the Natural Science Foundation of China (NSFC) (grants 11825403, 11991061, 12188101, and 12174060), and the Guangdong Major Project of the Basic and Applied Basic Research

(Future functional materials under extreme conditions–2021B0301030005). J.W. acknowledges support from NSFC (grant 12074164), Guangdong Innovative and Entrepreneurial Research Team Program (grant 2021ZT09C296), and Guangdong Provincial Key Laboratory Program (2021B1212040001) from the Department of Science and Technology of Guangdong Province. C.X. also acknowledges support from NSFC (grant 12274082) and support from Shanghai Science and Technology Committee (grant 23ZR1406600).

LITERATURE CITED

1. Schmid H. 1994. *Ferroelectrics* 162:317–38
2. Wang P, Xiang H. 2014. *Phys. Rev. X* 4:011035
3. Nan CW, Bichurin M, Dong S, Viehland D, Srinivasan G. 2008. *J. Appl. Phys.* 103(3):1
4. Dong S, Xiang H, Dagotto E. 2019. *Natl. Sci. Rev.* 6(4):629–41
5. Eerenstein W, Mathur N, Scott JF. 2006. *Nature* 442(7104):759–65
6. Cheong SW, Mostovoy M. 2007. *Nat. Mater.* 6:13–20
7. Ramesh R, Spaldin NA. 2007. *Nat. Mater.* 6:21–29
8. Wang K, Liu JM, Ren Z. 2009. *Adv. Phys.* 58(4):321–448
9. Fiebig M, Lottermoser T, Meier D, Trassin M. 2016. *Nat. Rev. Mater.* 1(8):1–14
10. Picozzi S, Yamauchi K, Sergienko IA, Sen C, Sanyal B, Dagotto E. 2008. *J. Phys.: Condens. Matter* 20(43):434208
11. Khomskii D. 2009. *Physics* 2:20
12. Wang J, Neaton J, Zheng H, Nagarajan V, Ogale S, et al. 2003. *Science* 299(5613):1719–22
13. Van Aken BB, Palstra TT, Filippetti A, Spaldin NA. 2004. *Nat. Mater.* 3(3):164–70
14. Kimura T, Goto T, Shintani H, Ishizaka K, Arima T, Tokura Y. 2003. *Nature* 426(6962):55–58
15. Hill NA. 2000. *J. Phys. Chem. B* 104(29):6694–709
16. Neaton J, Ederer C, Waghmare U, Spaldin N, Rabe K. 2005. *Phys. Rev. B* 71:014113
17. Johnston K, Huang X, Neaton JB, Rabe KM. 2005. *Phys. Rev. B* 71(10):100103
18. Wang C, Guo GC, He L. 2007. *Phys. Rev. Lett.* 99(17):177202
19. Picozzi S, Yamauchi K, Sanyal B, Sergienko IA, Dagotto E. 2007. *Phys. Rev. Lett.* 99(22):227201
20. Xiang H, Whangbo MH. 2007. *Phys. Rev. Lett.* 99(25):257203
21. Xiang H, Wei SH, Whangbo MH, Da Silva JL. 2008. *Phys. Rev. Lett.* 101(3):037209
22. Malashevich A, Vanderbilt D. 2008. *Phys. Rev. Lett.* 101(3):037210
23. Duan CG, Jaswal SS, Tsymbal EY. 2006. *Phys. Rev. Lett.* 97(4):047201
24. Luo W, Xu K, Xiang H. 2017. *Phys. Rev. B* 96(23):235415
25. Hubbard J. 1964. *Proc. R. Soc. Lond. Ser. A Math. Phys. Sci.* 277(1369):237–59
26. Xu C, Feng J, Kawamura M, Yamaji Y, Nahas Y, et al. 2020. *Phys. Rev. Lett.* 124(8):087205
27. Dzyaloshinsky I. 1958. *J. Phys. Chem. Solids* 4(4):241–55
28. Moriya T. 1960. *Phys. Rev.* 120:91
29. Xiang H, Kan E, Whangbo MH, Lee C, Wei SH, Gong X. 2011. *Phys. Rev. B* 83(17):174402
30. Liu J, Koo HJ, Xiang H, Kremer RK, Whangbo MH. 2014. *J. Chem. Phys.* 141(12):124113
31. Moriya T, Yosida K. 1953. *Prog. Theor. Phys.* 9(6):663–75
32. Ye F, Morgan Z, Tian W, Chi S, Wang X, et al. 2021. *Phys. Rev. B* 103(18):184413
33. Li X, Xu C, Liu B, Li X, Bellaiche L, Xiang H. 2023. *Phys. Rev. Lett.* 131:036701
34. Ni J, Li X, Amoroso D, He X, Feng J, et al. 2021. *Phys. Rev. Lett.* 127(24):247204
35. Gutzeit M, Kubetzka A, Haldar S, Pralow H, Goerzen MA, et al. 2022. *Nat. Commun.* 13:5764
36. Paul S, Haldar S, Von Malottki S, Heinze S. 2020. *Nat. Commun.* 11:4756
37. Xu C, Li X, Chen P, Zhang Y, Xiang H, Bellaiche L. 2022. *Adv. Mater.* 34(12):2107779
38. Novák P, Chaplygin I, Seifert G, Gemming S, Laskowski R. 2008. *Comput. Mater. Sci.* 44:79–81
39. Li X, Yu H, Lou F, Feng J, Whangbo MH, Xiang H. 2021. *Molecules* 26(4):803
40. Escorihuela-Sayalero C, Diéguez O, Íñiguez J. 2012. *Phys. Rev. Lett.* 109(24):247202
41. Yang H, Thiaville A, Rohart S, Fert A, Chshiev M. 2015. *Phys. Rev. Lett.* 115(26):267210

42. Yang H, Liang J, Cui Q. 2023. *Nat. Rev. Phys.* 5:43–61
43. Xiang H, Kan E, Wei SH, Whangbo MH, Gong X. 2011. *Phys. Rev. B* 84(22):224429
44. Xiang H, Lee C, Koo HJ, Gong X, Whangbo MH. 2013. *Dalton Trans*. 42(4):823–53
45. Xu C, Feng J, Prokhorenko S, Nahas Y, Xiang H, Bellaiche L. 2020. *Phys. Rev. B* 101(6):060404
46. Lu X, Wu X, Xiang H. 2015. *Phys. Rev. B* 91(10):100405
47. Li J, Feng J, Wang P, Kan E, Xiang H. 2021. *Sci. China Phys. Mech. Astron*. 64(8):286811
48. Lou F, Li X, Ji J, Yu H, Feng J, et al. 2021. *J. Chem. Phys.* 154(11):114103
49. Singer R, Dietermann F, Fähnle M. 2011. *Phys. Rev. Lett.* 107:017204
50. Li XY, Lou F, Gong XG, Xiang H. 2020. *New J. Phys.* 22(5):053036
51. Liechtenstein AI, Katsnelson M, Antropov V, Gubanov V. 1987. *J. Magnet. Magnet. Mater.* 67:65–74
52. Liechtenstein A, Anisimov VI, Zaanen J. 1995. *Phys. Rev. B* 52(8):R5467
53. Wan X, Yin Q, Savrasov SY. 2006. *Phys. Rev. Lett*. 97(26):266403
54. Korotin DM, Mazurenko V, Anisimov V, Streltsov S. 2015. *Phys. Rev. B* 91(22):224405
55. Antropov V, Katsnelson M, Liechtenstein A. 1997. *Phys. B: Condens. Matter* 237:336–40
56. Lounis S, Dederichs PH. 2010. *Phys. Rev. B* 82(18):180404
57. Szilva A, Costa M, Bergman A, Szunyogh L, Nordström L, Eriksson O. 2013. *Phys. Rev. Lett.* 111(12):127204
58. Solovyev I. 2021. *Phys. Rev. B* 103(10):104428
59. Andersen OK, Jepsen O. 1984. *Phys. Rev. Lett.* 53(27):2571
60. Rudenko A, Mazurenko V, Anisimov V, Lichtenstein A. 2009. *Phys. Rev. B* 79(14):144418
61. Katsnelson M, Lichtenstein A. 2000. *Phys. Rev. B* 61(13):8906
62. Katsnelson M, Kvashnin Y, Mazurenko V, Lichtenstein A. 2010. *Phys. Rev. B* 82(10):100403
63. Solovyev I, Hamada N, Terakura K. 1996. *Phys. Rev. Lett.* 76(25):4825
64. Yavorsky BY, Mertig I. 2006. *Phys. Rev. B* 74(17):174402
65. He X, Helbig N, Verstraete MJ, Bousquet E. 2021. *Comput. Phys. Commun.* 264:107938
66. Kotliar G, Savrasov SY, Haule K, Oudovenko VS, Parcollet O, Marianetti C. 2006. *Rev. Mod. Phys.* 78(3):865
67. Durhuus FL, Skovhus T, Olsen T. 2023. *J. Phys.: Condens. Matter* 35(10):105802
68. Blöchl PE. 1994. *Phys. Rev. B* 50(24):17953
69. King-Smith R, Vanderbilt D. 1993. *Phys. Rev. B* 47(3):1651
70. Resta R. 1994. *Rev. Mod. Phys.* 66(3):899
71. Berry MV. 1984. *Proc. R. Soc. Lond. A Math. Phys. Sci.* 392(1802):45–57
72. Baroni S, De Gironcoli S, Dal Corso A, Giannozzi P. 2001. *Rev. Mod. Phys.* 73(2):515
73. Gonze X. 1997. *Phys. Rev. B* 55(16):10337
74. Souza I, Íniguez J, Vanderbilt D. 2002. *Phys. Rev. Lett.* 89(11):117602
75. Umari P, Pasquarello A. 2002. *Phys. Rev. Lett.* 89(15):157602
76. Stengel M, Spaldin NA, Vanderbilt D. 2009. *Nat. Phys.* 5(4):304–8
77. Zhong W, Vanderbilt D, Rabe K. 1995. *Phys. Rev. B* 52(9):6301
78. Wojdeł JC, Hermet P, Ljungberg MP, Ghosez P, Íñiguez J. 2013. *J. Phys.: Condens. Matter* 25(30):305401
79. Kornev IA, Lisenkov S, Haumont R, Dkhil B, Bellaiche L. 2007. *Phys. Rev. Lett.* 99(22):227602
80. Wang D, Weerasinghe J, Bellaiche L. 2012. *Phys. Rev. Lett.* 109(6):067203
81. Agrawal A, Choudhary A. 2016. *APL Mater.* 4(5):053208
82. Carleo G, Cirac I, Cranmer K, Daudet L, Schuld M, et al. 2019. *Rev. Mod. Phys.* 91(4):045002
83. Pinheiro M, Ge F, Ferré N, Dral PO, Barbatti M. 2021. *Chem. Sci.* 12(43):14396–413
84. Schleder GR, Padilha AC, Acosta CM, Costa M, Fazzio A. 2019. *J. Phys.: Mater.* 2(3):032001
85. Joshi CK, Bodnar C, Mathis SV, Cohen T, Liò P. 2023. arXiv:2301.09308
86. Xie T, Grossman JC. 2018. *Phys. Rev. Lett.* 120(14):145301
87. Batzner S, Musaelian A, Sun L, Geiger M, Mailoa JP, et al. 2022. *Nat. Commun.* 13:2453
88. Musaelian A, Batzner S, Johansson A, Sun L, Owen CJ, et al. 2023. *Nat. Commun.* 14:579
89. Eckhoff M, Behler J. 2021. *npj Comput. Mater.* 7:170
90. Yu H, Xu C, Li X, Lou F, Bellaiche L, et al. 2022. *Phys. Rev. B* 105(17):174422
91. Yu H, Zhong Y, Ji J, Gong X, Xiang H. 2022. arXiv:2211.11403

92. Chapman JB, Ma PW. 2022. *Sci. Rep.* 12:22451
93. Domina M, Cobelli M, Sanvito S. 2022. *Phys. Rev. B* 105(21):214439
94. Egorov A, Subramanyam A, Yuan Z, Drautz R, Hammerschmidt T. 2023. *Phys. Rev. Mater.* 7:044403
95. Nikolov S, Wood MA, Cangi A, Maillet JB, Marinica MC, et al. 2021. *npj Comput. Mater.* 7:153
96. Novikov I, Grabowski B, Körmann F, Shapeev A. 2022. *npj Comput. Mater.* 8:13
97. Thompson AP, Swiler LP, Trott CR, Foiles SM, Tucker GJ. 2015. *J. Comput. Phys.* 285:316–30
98. Yu H, Zhong Y, Xu C, Gong X, Xiang H. 2022. arXiv:2203.02853
99. Sergienko IA, Dagotto E. 2006. *Phys. Rev. B* 73(9):094434
100. Mostovoy M. 2006. *Phys. Rev. Lett.* 96(6):067601
101. Katsura H, Nagaosa N, Balatsky AV. 2005. *Phys. Rev. Lett.* 95(5):057205
102. Arima T. 2007. *J. Phys. Soc. Jpn.* 76(7):073702
103. Jia C, Onoda S, Nagaosa N, Han JH. 2006. *Phys. Rev. B* 74(22):224444
104. Xiang H, Kan E, Zhang Y, Whangbo MH, Gong X. 2011. *Phys. Rev. Lett.* 107(15):157202
105. Lu X, Whangbo MH, Dong S, Gong X, Xiang H. 2012. *Phys. Rev. Lett.* 108(18):187204
106. Xiang H, Wang P, Whangbo MH, Gong X. 2013. *Phys. Rev. B* 88(5):054404
107. Yang JH, Li ZL, Lu X, Whangbo MH, Wei SH, et al. 2012. *Phys. Rev. Lett.* 109(10):107203
108. Dzyaloshinskii IE. 1960. *Sov. Phys. JETP* 10:628–29
109. Íniguez J. 2008. *Phys. Rev. Lett.* 101(11):117201
110. Ye M, Vanderbilt D. 2014. *Phys. Rev. B* 89(6):064301
111. Bousquet E, Spaldin NA, Delaney KT. 2011. *Phys. Rev. Lett.* 106(10):107202
112. Xu K, Feng J, Xiang H. 2022. *Chinese Phys. B* 31(9):097505
113. Malashevich A, Souza I, Coh S, Vanderbilt D. 2010. *New J. Phys.* 12(5):053032
114. Essin AM, Turner AM, Moore JE, Vanderbilt D. 2010. *Phys. Rev. B* 81(20):205104
115. Malashevich A, Coh S, Souza I, Vanderbilt D. 2012. *Phys. Rev. B* 86(9):094430
116. Scaramucci A, Bousquet E, Fechner M, Mostovoy M, Spaldin NA. 2012. *Phys. Rev. Lett.* 109(19):197203
117. Seifert H, Uebach J. 1981. *Z. Anorg. Allg. Chem.* 479(8):32–40
118. Hillebrecht H, Schmidt P, Rotter H, Thiele G, Zönnchen P, et al. 1997. *J. Alloys Compd.* 246(1–2):70–79
119. Ai H, Song X, Qi S, Li W, Zhao M. 2019. *Nanoscale* 11(3):1103–10
120. Xu C, Chen P, Tan H, Yang Y, Xiang H, Bellaiche L. 2020. *Phys. Rev. Lett.* 125(3):037203
121. Zhong T, Li X, Wu M, Liu JM. 2020. *Natl. Sci. Rev.* 7(2):373–80
122. Zhang J, Shen X, Wang Y, Ji C, Zhou Y, et al. 2020. *Phys. Rev. Lett.* 125:017601
123. Ji J, Xu C, Xiang H. 2023. *Phys. Rev. Lett.* 130:146801
124. Tan H, Li M, Liu H, Liu Z, Li Y, Duan W. 2019. *Phys. Rev. B* 99(19):195434
125. Ding N, Chen J, Dong S, Stroppa A. 2020. *Phys. Rev. B* 102(16):165129
126. Peng J, Liu Y, Lv H, Li Y, Lin Y, et al. 2021. *Nat. Chem.* 13(12):1235–40
127. Zhao Y, Liu Q, Zhang F, Jiang X, Gao W, Zhao J. 2022. *J. Phys. Chem. Lett.* 13(48):11346–53
128. Lu J, Luo W, Feng J, Xiang H. 2018. *Nano Lett.* 18:595–601
129. Zhang J, Zhou Y, Wang F, Shen X, Wang J, Lu X. 2022. *Phys. Rev. Lett.* 129(11):117603
130. Shen X, Wang F, Lu X, Zhang J. 2023. *Nano Lett.* 23(2):735–41
131. Ji D, Cai S, Paudel TR, Sun H, Zhang C, et al. 2019. *Nature* 570(7759):87–90
132. Li L, Wu M. 2017. *ACS Nano* 11(6):6382–88
133. Lei C, Chittari BL, Nomura K, Banerjee N, Jung J, MacDonald AH. 2021. *Nano Lett.* 21(5):1948–54
134. Liu X, Pyatakov AP, Ren W. 2020. *Phys. Rev. Lett.* 125(24):247601
135. Tong WY, Gong SJ, Wan X, Duan CG. 2016. *Nat. Commun.* 7:13612
136. Ju H, Lee Y, Kim KT, Choi IH, Roh CJ, et al. 2021. *Nano Lett.* 21(12):5126–32
137. Song Q, Occhialini CA, Ergeçen E, Ilyas B, Amoroso D, et al. 2022. *Nature* 602(7898):601–5
138. Kurumaji T, Seki S, Ishiwata S, Murakawa H, Kaneko Y, Tokura Y. 2013. *Phys. Rev. B* 87:014429
139. Zhang JJ, Lin L, Zhang Y, Wu M, Yakobson BI, Dong S. 2018. *J. Am. Chem. Soc.* 140(30):9768–73
140. Su Y, Li X, Zhu M, Zhang J, You L, Tsymbal EY. 2020. *Nano Lett.* 21:175–81
141. Kuindersma S, Sanchez J, Haas C. 1981. *Physica B+C* 111(2–3):231–48
142. Okubo T, Chung S, Kawamura H. 2012. *Phys. Rev. Lett.* 108:017206
143. Amoroso D, Barone P, Picozzi S. 2020. *Nat. Commun.* 11:5784

144. Riedl K, Amoroso D, Backes S, Razpopov A, Nguyen TPT, et al. 2022. *Phys. Rev. B* 106(3):035156
145. Ni Xs, Yao DX, Cao K. 2022. arXiv:2209.12392
146. Tokunaga Y, Okuyama D, Kurumaji T, Arima T, Nakao H, et al. 2011. *Phys. Rev. B* 84(6):060406
147. Kurumaji T, Seki S, Ishiwata S, Murakawa H, Tokunaga Y, et al. 2011. *Phys. Rev. Lett.* 106(16):167206
148. Lu Y, Fei R, Lu X, Zhu L, Wang L, Yang L. 2020. *ACS Appl. Mater. Interfaces* 12(5):6243–49
149. Runge E, Gross EK. 1984. *Phys. Rev. Lett.* 52(12):997